Published in final edited form as:

Structure. 2021 June 03; 29(6): 540–552.e5. doi:10.1016/j.str.2020.12.013.

Structures of FHOD1-Nesprin1/2 complexes reveal alternate binding modes for the FH3 domain of formins

Sing Mei Lim[1], **Victor E. Cruz**[1], **Susumu Antoku**[2], **Gregg G. Gundersen**[1], **Thomas U. Schwartz**[1,3,*]

[1]Department of Biology, Massachusetts Institute of Technology, Cambridge, Massachusetts 02139, USA

[2]Department of Pathology and Cell Biology, Columbia University, New York, New York 10032, USA

[3]Lead Contact

SUMMARY

The nuclear position in eukaryotes is controlled by a nucleo-cytoskeletal network, critical in cell differentiation, division and movement. Forces are transmitted through conserved Linker of Nucleoskeleton and Cytoskeleton (LINC) complexes that traverse the nuclear envelope and engage on either side of the membrane with diverse binding partners. Nesprin-2-giant (Nes2G), a LINC element in the outer nuclear membrane, connects to the actin directly as well as through FHOD1, a formin primarily involved in actin-bundling. Here, we report the crystal structure of Nes2G bound to FHOD1 and show that the presumed G-binding domain of FHOD1 is rather a spectrin repeat (SR) binding enhancer for the neighboring FH3 domain. The structure reveals that SR binding by FHOD1 is likely not regulated by the DAD helix of FHOD1. Finally, we establish that Nes1G also has one FHOD1 binding SR, indicating that these abundant, giant Nesprins have overlapping functions in actin-bundle recruitment for nuclear movement.

Graphical Abstract

*Corresponding author: tus@mit.edu.

AUTHOR CONTRIBUTIONS

S.M.L. and T.U.S. designed the study. S.M.L. and V.E.C. performed the experiments. G.G.G. and S.A. contributed Figure 4 and Figure S5. S.M.L. and T.U.S. interpreted the results and wrote the manuscript with input from G.G.G., S.A., and V.E.C.

DECLARATION OF INTERESTS

The authors declare no competing interests.

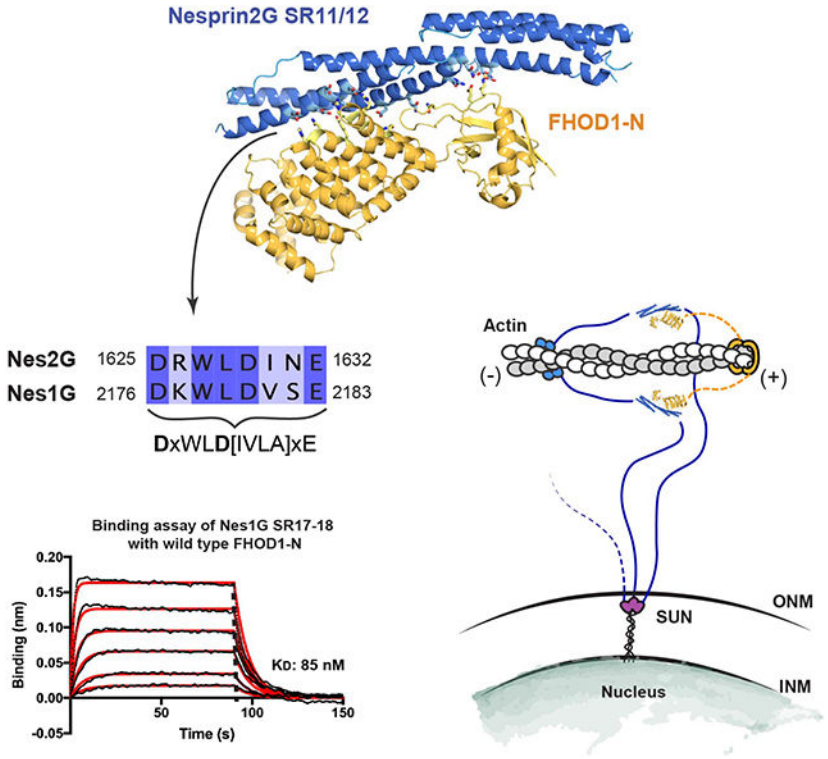

eTOC Blurb

Nuclear movement depends on LINC complexes — physical, nucleo-cytoplasmic connections across the nuclear envelope. Lim et al. reveal, employing crystallographic, biochemical, and cell biological tools, how Nesprin-1 and -2, KASH proteins of the LINC complex, interact with cytosolic FHOD1 to connect to actin cables.

Keywords

Formin homology domain protein FHOD1; LINC complex; Nesprin; nuclear movement; spectrin repeat; Transmembrane actin associated nuclear (TAN) lines; actin bundling; nucleoskeleton; cytoskeleton; diaphanous-related formin homology domain - FH3 domain

INTRODUCTION

Eukaryotic cells in multicellular organisms display an enormous range of specialization. The development of different tissues coincides with cellular reorganization, often involving large rearrangements of organelles. The position of the nucleus as the largest organelle is often found to be a distinct marker for certain cell types, for example in muscle cells or in neurons (Gundersen and Worman, 2013). During nuclear migration, the nucleus interacts with the cytoskeletal network for active positioning. Pulling forces across the nuclear envelope are primarily mediated by a two-protein complex known as Linker of Nucleoskeleton and Cytoskeleton (LINC) (Crisp et al., 2006; Starr and Fridolfsson, 2010). LINC complexes are universally conserved in eukaryotes and consist of Klarsicht/ANC-1/Syne homology

(KASH) proteins that transverse the outer nuclear membrane (ONM), and Sad1-UNC84 (SUN) proteins which pass through the inner-nuclear membrane (INM) and connect to the nucleoskeleton. In the perinuclear space, three SUN domains interact with three C-terminal KASH peptides of Nesprins to form an intricate heterohexameric assembly(Sosa et al., 2012), the core of the LINC complex. Humans have five known SUN proteins and six KASH-containing proteins (Lindeman and Pelegri, 2012; Mellad et al., 2011; Morimoto et al., 2012; Noegel and Neumann, 2011; Rothballer and Kutay, 2013). Some of these SUN- and KASH-proteins are ubiquitously expressed, while some are tissue specific (Rothballer and Kutay, 2013). They generate a diverse network of nucleo-cytoplasmic linkages that are important for homeostasis and trigger multiple genetic diseases, if altered (Calvi and Burke, 2015; Horn, 2014; Janin et al., 2017). The regulation and the interplay between the different LINC complexes are important elements in deciphering the entire network.

In the migrating fibroblasts, the nuclear position depends on nesprin-2 giant (Nes2G), a large, actin-binding LINC component of transmembrane actin-associated (TAN) lines(Luxton et al., 2010). FHOD1 is a formin that itself binds and bundles actin, while also interacting with Nes2G (Kutscheidt et al., 2014) This way, an interaction network between actin bundles, Nes2G, and FHOD1 is established.

The molecular details of this intricate connection are largely unknown, in no small part because the proteins involved are complicated, multi-domain entities. The 800 kDa Nes2G contains two N-terminal, actin-interacting calponin homology (CH) domains followed by 56 spectrin repeats (SRs) before the ONM-transversing transmembrane-helix and the C-terminal KASH peptide, that interacts with SUN1/2 (Rajgor and Shanahan, 2013; Zhang et al., 2001). Formins are categorized into several classes dependent on their function and domain architecture (Breitsprecher and Goode, 2013; Higgs, 2005; Pruyne, 2017; Rivero et al., 2005). Formin homology domain protein, FHOD1 is the founding member of one class, with an N-terminal, presumed G-protein binding domain (G2 or GBD2), followed by a diaphanous-related formin homology domain, FH3 or also known as diaphanous inhibitory domain (DID) that is autoinhibited through intramolecular interaction with a conserved C-terminal diaphanous-autoregulatory domain (DAD) (Bechtold et al., 2014). Between FH3 and DAD, FHOD1 also contains a profilin binding proline-rich FH1 domain and the actin-bundling FH2 domain, central to all formins (Higgs and Peterson, 2004; Pruyne, 2017; Romero et al., 2004). Another large class of formins are the diaphanous-related formins (DRFs). They contain a tested, structurally different GBD N-terminal to the FH3 (Kühn et al., 2015; Lammers et al., 2008).

We sought to advance our mechanistic understanding of the emerging, functionally important actin-Nes2G FHOD1 network. In this study, we determined the crystal structure of Nes2G SR11–12 in complex with FHOD1, revealing a formin-binding motif within spectrin repeats. Using a bioinformatic analysis we detect that Nes1G also carries this formin-binding motif in one out of its 76 SRs, which we confirm with structural and biochemical methods. SR11–12 binding by FHOD1 is outside of the autoregulation through DAD and independent of actin bundling. Further, we establish that the small domain preceding the FH3 domain of FHOD1, formerly GBD2 or G2, is in fact a modulator of

the binding specificity of the neighboring FH3 domain, making the paired domain specific for SR, rather than GTPase interaction.

RESULTS

Crystal structure of Nes2G SR11–12 in complex with FHOD1-N

We set out to characterize how Nes2G interacts with the N-terminal GBD-FH3 domain element of FHOD1 structurally. This is based on a previous study where specific Nes2G SRs and FHOD1 domains have been identified (Kutscheidt et al., 2014). We recombinantly expressed spectrin repeats SR 11–12 of human Nes2G (residues 1425–1649), Nes2G SR11–12, as well as FHOD1-N (residues 1–339) (Figure 1A). Both proteins form a stable 1:1 complex (Figure S1A), with a measured K_D of 375 nM (Figure S1B). While we initially worked with a cysteine double-mutant, FHOD1-N (C31S C71S), based on the report that wild-type FHOD1-N has a tendency to form artificial, cysteine-mediated dimers in solution (Schulte et al., 2008). we did not observe the reported behavior (Figure S2). Therefore, we continued our studies with wild-type FHOD1-N.

We obtained crystals of the Nes2G SR11–12-FHOD1-N that diffracted to 2.8 Å resolution. The crystals belong to space group C2 and contain two heterodimeric complexes per asymmetric unit. One of the two complexes is better packed and therefore better resolved. Both complexes superpose well with a root mean square deviation (RMSD) of 0.82 Å. Nes2G SR11–12 adopts the canonical structure of a tandem SR, i.e. two antiparallel coiled-coils connected by a continuous α-helix, generating two tethered three-helix bundles with a left-handed twist (Figure 1B). FHOD1-N superposes well with the apo-structure (Schulte et al., 2008) with an RMSD of 1.08 Å (Figure S1C). The FH3 domain (residues 115–339) is an α-helical solenoid composed of five armadillo repeats. It is immediately preceded by a small domain (residues 14–114) that has a ubiquitin superfold. Formerly described as a GTPase-binding domain, we refer to this domain as an SR-binding module (SRBM), as it will become clear further on. The most significant difference between apo- and Nes2G bound FHOD1-N is the ordering of a surface loop in the SRBM domain, residues 30–40, upon binding.

FHOD1-N engages with the tandem SR by generating a continuous binding surface along the long axis of the helical bundle. In total, the binding interface buries 1191 $Å^2$. The majority of the interaction is between the FH3 domain and SR12, with additional contributions from the SRBM and the long, SR11-SR12 connecting central helix. As it is typical for protein-protein interactions, we see a mix of van der Waals, polar and charged interactions throughout the interface. Two areas within the binding interface stand out, referred to as site A and site B (Figures 1B – 1E). Site A is the core interface, centered around a remarkable charge network. D1625, D1629, and E1632 of Nes2G SR12 form a web of salt bridges with R136 and R137 of FHOD1-N (Figure 1C). The hydrophobic residues L1628 of Nes2G SR12 and F140 of FHOD1-N get deeply buried in the site A interface upon binding. A number of additional hydrogen-bonds surround and complete this site (Figures S3 and S4). All the key residues in site A are very well conserved across diverse species, supporting the notion that this is an important functional interface (Figures S3 and S4).

Site B involves the loop connecting strands β1 and β2 of FHOD1-SRBM, particularly residues 30–38, interacting primarily with the very N-terminal α-helical element Nes2G SR12 (residues 1525–1532). The FHOD1-SRBM-loop packs against the SR12 helical bundle and becomes well-ordered, in contrast to its more flexible position in the apo-form. A hydrogen-bonding / charge network is formed between E36 and R38 of FHOD1-SRBM and E1528 and Q1529 of Nes2G SR12, with the best ordered water molecule of the structure as an integral component (Figure 1E). Several exposed, hydrophobic residues get buried upon binding (A32, F34 of FHOD1-SRBM and F1603 of Nes2G SR12) (Figures S3 and S4).

Of note, the FH3 and the SRBM domain largely retain their relative orientation upon SR-binding, as evidenced by the superposition of apo- onto bound FHOD1 form (Figure S1). We attribute this to the fairly extensive domain contacts between FH3 and SRBM, already noticed in the apo-form (Schulte et al. 2008)

Mutations in residues of Nes2G FHOD1 interaction interface abolish protein complex formation

In order to determine which residues are most critical for the interaction, and to generate meaningful point-mutations for biological assays, we analyzed the effect of mutating conserved interacting residues. We probed for complex formation by size exclusion chromatography (SEC) and bio-layer interferometry (BLI) (Figure 2). In site A, we determined that the charge network is essential for binding, since a Nes2G SR11–12 D1625A/D1629A double mutant abolished binding in the SEC assay. Mutating the paired, charged residues on FHOD1-N, R136A and R137A, expectedly, has the same effect (Figures 2B – 2D). The hydrophobic interaction between Nes2G SR11–12 L1628 and FHOD1-N F140 is also essential. A Nes2G SR11–12 L1628R or Nes2G SR11–12 L1628A E1632A mutant abolishes binding as well (Figures 2A and 2C). We also analyzed site B, probing it with a FHOD1-N SRBM-loop triple mutant E36A P37G R38A. SEC and BLI both still show residual binding, suggesting that site B is perhaps somewhat less critical than site A (Figures 2B – 2D). In summary, we establish Nes2G D1625A D1629A and FHOD1 R136A R137A as structurally defined, non-interacting probes for *in vitro* and *in vivo* studies.

Disruption of FHOD1-Nes2G interaction blocks nuclear movement

It is known that FHOD1 and Nes2G functionally interact to reposition the nucleus rearward in fibroblasts during polarity establishment for cell migration (Antoku et al., 2015; Kutscheidt et al., 2014). We examined the effect of FHOD1-Nes2G interaction site mutants on the rearward movement of nuclei in wound-edge fibroblasts stimulated with lysophosphatidic acid (LPA). Previously, we showed that expression of Nes2G SR11–13 in fibroblast inhibited LPA-stimulated nuclear movement (Antoku et al., 2019). Similar to the earlier result, expression of the shorter Nes2G SR11–12 inhibited rearward nuclear movement and polarity establishment as measured by centrosome orientation (Figures 3A, 3B, and S5A). In contrast, expression of Nes2G D1625A D1629A, which does not interact with FHOD1, did not inhibit nuclear movement or centrosome orientation (Figures 3A, 3B, and S5A). This indicates that the dominant negative effect of Nes2G SR11–12 on nuclear movement requires binding activity with FHOD1.

Next, we examined FHOD1 interaction site mutants. As shown previously, (Kutscheidt et al., 2014), re-expression of wild-type FHOD1 in cells depleted of FHOD1 rescues their defects in nuclear movement and centrosome orientation (Figures 3C, 3D, and S5B). Unlike wild-type FHOD1, expression of FHOD1 R136A R137A or E36A P37G R38A in FHOD1 knockdown cells did not rescue their nuclear movement and centrosome orientation defects, similar to the inability of the actin-binding defective mutant I705A to rescue these phenotypes in FHOD1-depleted cells (Figures 3C, 3D, and S5B). To examine whether the R136A/R137A and E36A P37G R38A mutations affected FHOD1's actin activity, we looked at the ability of FHOD1 to colocalize with F-actin in cells. For this experiment, we used the constitutively active form of FHOD1, FHOD1 ΔDAD, which localizes to F-actin bundles in cells (Takeya and Sumimoto, 2003) (Figure S5C). Both R136A R137A and E36A P37G R38A mutants of FHOD1 ΔDAD colocalized with actin cables in cells, although the R136A R137A mutant appeared to be somewhat reduced compared to wild-type (Figure S5C). These results suggest that the Nes2G interaction site mutations of FHOD1 primarily affect Nes2G's actin binding, but not FHOD1's own actin activity. Together these results strongly argue that the FHOD1-Nes2G interaction revealed by the crystal structure is essential for function in cells.

The FHOD1 binding motif is also found in Nesprin-1G

Having established how FHOD1-N interacts with Nes2G SR11–12 we asked whether the motif we identified might be found in other spectrin repeat proteins as well. Based on our mutational study, we identified DxWLD[IVLA]xE to be a signature motif within a spectrin repeat that would suggest FHOD1-binding. By using BLAST pattern search, we found this motif in one other spectrin repeat containing actin binding protein, namely Nesprin-1-Giant (Nes1G). Nes1G is also part of LINC complexes, with a C-terminal KASH-peptide that interacts with Sun1/2. Similar to Nes2G, the N terminus of Nes1G has two actin-binding CH domains followed by many (74 vs 56) SRs (Duong et al., 2014) We found the motif to be 100% conserved in Nes1G SR18 (Figures 4A and S6A).

To test the functionality of Nes1G SR18 as an FHOD-1 interactor, we expressed and purified the tandem SR repeat Nes1G SR17–18 (residues 1976–2200) recombinantly in *E. coli* and analyzed FHOD1-N binding by SEC and BLI. FHOD1-N and Nes1G SR17–18 coelute from a SEC column as a complex with 1:1 stoichiometry (Figure 4B). We measured a binding affinity between Nes1G SR17–18 and FHOD1-N of 85 nM, comparable to that of Nes2G SR11–12 (375 nM, Figure S1) under the same buffer condition (Figure 4C). Further pointing to the same binding interaction, when the aspartate residues were mutated in the DxWLD[IVLA]xE motif or the corresponding R136A R137A mutations introduced into FHOD1-N, Nes1G SR17–18 no longer binds to FHOD1-N (Figures 4D–4E).

Structure of Nes1G SR17–18 with FHOD1-N

We obtained crystals of Nes1G SR17–18 in complex with FHOD1-N that diffracted to 7 Å resolution. The structure was solved by molecular replacement using the Nes2G SR11–12-FHOD1-N complex as the search model. The crystals also belong to the C2 space group, with two complexes per asymmetric unit. Due to the modest resolution, we only used rigid body refinement to position the four domain elements, Nes1G SR17, Nes1G SR18, FHOD1-

SRBM, and FHOD1-FH3. Nes1G SR17 is essentially invisible in the density, suggesting disorder (Figures 5A and S6B). The other three domain elements superpose very well with the Nes2G SR12-FHOD1-N complex. In order to verify whether SR17 is dispensable for FHOD1-N interaction, we analyzed a Nes1G SR18-only construct (residues 2076–2200) for FHOD1-N binding. We found stable FHOD1-N interaction with Nes1G SR18 as analyzed by SEC and BLI (Figures 5B – 5C).

Binding of Nes2G does not preclude FHOD1-autoinhibition

Actin bundling by FHOD1-N is autoinhibited by its C-terminal DAD-helix binding to the FH3 domain (Higgs, 2005; Nezami et al., 2006). This autoinhibition can be released by phosphorylation of various serine and threonine residues within the DAD-helix by Rho kinase (Gasteier et al., 2003; Takeya et al., 2008). Since both, Nes2G SR11–12 and DAD can bind to the FH3 domain, we tested whether they compete with one another. While the DAD binding site is not structurally known for FHOD1, it can be predicted with great confidence. The superposition of the FH3 domain of mDia bound to its DAD-helix (PDB code 2F31) (Nezami et al., 2006) onto FHOD1-FH3 suggests a position, that is functionally confirmed by mutational analysis. A V228E mutation on the surface of FHOD1-FH3, predicted to be in the core of the DAD-binding site, potently blocks DAD-binding *in vitro* (Schulte et al., 2008). Modelling a putatively bound DAD-helix onto the Nes2G SR11–12-FHOD1-N complex suggests that the two interactions are independent and not in steric conflict (Figure 6A). To test this experimentally we co-incubated Nes2G SR11–12-FHOD1-N complex with an MBP-tagged 3C-cleavable DAD-helix fusion. To avoid steric hindrance by the MBP-fusion tag we cleaved the tag with 3C protease. As expected, we detect DAD-helix coeluting with the Nes2G SR11–12-FHOD1-N complex, indicating that the two binding sites are independent (Figure 6B). It further suggests that FHOD1 autoinhibition does not regulate Nes1G or Nes2G binding (Antoku et al., 2015; Otomo et al., 2010)

FHOD1 has a spectrin-repeat binding modulator (SRBM) rather than a GTPase-binding domain

Phylogenetic analysis revealed that the FH3 or DID domain in formins is preceded by one of two small domains, either a GTPase-binding domain (GBD or G) or the SRBM described here (formerly GBD2 or G2). Several crystal structures of the tethered GBD-FH3 domain in complex with small GTPases exist from diverse species, and the binding mode is very similar. Both the GBD domain and the FH3 domain contribute to the GTPase interaction (Figure 7A)(Kühn et al., 2015; Lammers et al., 2008). In comparison, the tethered SRBM-FH3 domain instead binds SRs, also with contributions from both domain elements (Figure 7B). When we phylogenetically analyzed maximally diverged SRBM-FH3 sequences and compared them with equally diverged GBD-FH3 sequences we detected distinct conservation of key residues within the respective binding sites of the FH3 domain (Figure 7). For example, positions 144 and 189 of FHOD1, strongly conserved as glutamine and leucine, respectively, in the SRBM-FH3 family, are instead strongly conserved as valine and asparagine in the GBD-FH3 family (Figure S7D). Conversely, the pair of invariant arginines in position 136 and 137 of FHOD1, important for SR recognition, are not at all conserved in the GBD-FH3 family (Figure S7H). This result clearly suggests that the FH3 domain has evolved to either bind a small GTPase or SRs, depending on which domain,

SRBM or G, it is tethered to. In other words, SRBM or G modulate the binding activity of the neighboring FH3 domain.

DISCUSSION

Here we show how FHOD1-N engages with SRs from two nesprins to form stable complexes. How does this structure inform us about tethering between the nucleus and actin bundles during nuclear migration along TAN lines? One important factor is how to achieve stability within this protein network. We propose that this is established through a multitude of interactions with actin. Specifically, Nesprin-2 has two N-terminal CH domains each of which directly bind actin filaments. Furthermore, SR11–12 engages with FHOD1, which bundles actin through its FH2 domain. Since FHOD1 itself is a dimer, this tethered FHOD1-Nes2G heterotetrameric unit then already has 6 individual actin binding sites (Figure 8A). Due to avidity, this arrangement should greatly increase actin filament affinity, a prerequisite for sustaining the large mechanical forces associated with moving such a gigantic cargo. This is also compatible with a model of Nesprins-1/2 tethering together neighboring actin filaments to reinforce bundling in a TAN line assembly (Figure 8B) (Schönichen et al., 2013).

This structure is a snapshot along the path toward understanding the entire TAN line network. Much remains to be discovered to mechanistically understand the whole process of actin-dependent nuclear migration. One important element to consider going forward is the significance of FHOD1 binding to primarily just one SR in both, Nes1G and Nes2G. With these giant nesprins containing 74 and 56 SRs, respectively, is there significance in the position of the interacting SR? Going forward, an interesting experiment will be to shuffle the position of the FHOD1 binding site within these long SR proteins and see which effect this may have. The existing data strongly suggest that the position is critical. Our structures reveal that FHOD1 binds to specific SRs that share the conserved sequence motif DxWLD[IVLA]xE which we discovered. Therefore, the position of the cognate SR within a nesprin should matter. An alternative hypothesis would be that the number of binding sites rather than the position within a nesprin is important. This is also a testable scenario.

The crystal structure of a nesprin SR domain confirms that Nes2G SR11–12 shares, as expected from modeling, strong structural homology with the canonical SR architecture, as seen in α- and β-spectrin (Figures S8A–S8B). The main interaction with FHOD1 is mediated through a binding interface which has a distinct sequence motif DxWLD[IVLA]xE, found in Nes2G SR12 and Nes1G SR18, respectively. Binding by Nes1G and Nes2G is very similar, except that for Nes2G the interface also includes a short element of the preceding SR11. For Nes1G, SR17 is dispensable. While one could formally argue that in Nes2G a tandem SR is recognized while in Nes1G a single SR is sufficient, we would consider this to be an exaggeration of the actual differences. The SR11 element bound by FHOD1 is merely through the shared central helix that connects SR11 and SR12 and defining the exact domain boundary between the two is to an extent somewhat arbitrary. Structural information of other SRs protein and their binding partners is limited to β-spectrin – ankyrin complexes, specifically, crystal structures of human erythroid β-spectrin bound to single- or multi-domain ankyrin repeats (Ipsaro and Mondragón, 2010; Li et al., 2020). Here,

the interface with ankyrin clearly spans two neighboring SRs, where the relative orientation of the repeats is important. The binding itself is very different from the FHOD1-SR interface —not surprising given that FHOD1 and ankyrin have entirely different domain architectures (Figures S8C – S8D).

We now establish that the formerly named G2 or GBD2 domain of FHOD1 is a spectrin repeat binding modulator, which we call SRBM. It is another remarkable example of how nature has coopted a common domain fold, here ubiquitin, to evolve a different function. This common theme has been seen in many other folds, including helix-turn-helix motifs, β-propeller proteins, to name just a few (Aravind et al., 2005; Smith, 2008). The distinct evolution of the SRBM within the larger formin family has been recognized before based on phylogenetic analysis (Pruyne, 2017). However, it remained nearly unchallenged that this domain may not bind a small GTPase. While convinced about our biochemical, structural, and phylogenetic analysis consistently suggesting that the former G2 domain is an SRBM, we nevertheless also tested FHOD1-N binding to the small GTPase Rac1 (Figure S9), which was previously suggested to interact with FHOD1 (Schulte et al., 2008). Using a BLI assay, we registered no interaction of GMP-PNP bound Rac1 with immobilized FHOD1-N even at a concentration as high as 10 μM (Figure S9B). Further, we did also not observe any competition for FHOD1-N binding, neither with Nes2G SR17–18 nor Nes1G SR11–12 (Figures S9C and S9D). Our work provides another powerful example for why experimental validation is a critical element of discovery. Divergent evolution of domains into diverse functions can be difficult to discern, especially if these functions do not correlate with an easily recognizable sequence pattern.

The SRBM is not an autonomous domain that has its separable function. It appears to only function in tandem with the neighboring FH3 domain, which is why we call it a modulator. Neither FH3, nor SRBM bind a spectrin repeat independently. The sequence conservation of the SRBM supports this notion. The best conserved part within the SRBM is the long loop connecting β1 and β2, which is precisely necessary to lock the module with the FH3 domain and also to directly bind the cognate SR. Furthermore, neighboring SRBM and FH3 domains coevolved to bind spectrin repeats, which is evident when one compares the FHOD class of formins (Figure 7). The situation is not very different for the bona fide GBD, which is found in the larger class of diaphanous-related formins (DRFs). As shown previously, it also binds small GTPases in conjunction with the neighboring FH3 and apparently not autonomously (Kühn et al., 2015; Lammers et al., 2008). In the DRFs, the GBD co-evolved with the neighboring FH3 in much the same way as SRBM co-evolved with its joint FH3. This is clearly evident in the Pfam protein family database, where the GBD is defined as containing about half of the FH3 domain (Pfam entry 06371), with conserved residues distributed over both structural elements. Taken together, we suggest that GBD and SRBM are two, mutually exclusive modulators of the FH3 domain that direct and specify its binding activity. Perhaps, it is no coincidence that the FH3 domain is an α-solenoid, a versatile domain found in many, highly diverse protein assemblies.

STAR METHODS

RESOURCE AVAILABILITY

Lead Contact—Further information and requests for resources and reagent should be directed to and will be fulfilled by the Lead contact, Thomas U. Schwartz (tus@mit.edu).

Materials Availability—Plasmids and other material generated in the course of this study can be requested from the Lead contact, Thomas U. Schwartz (tus@mit.edu)

Data and Code Availability—The atomic coordinates and structure factors file for both structures have been deposited to and validated by the RCSB Protein Data Bank (http://www.wwpdb.org) with the following accession code: 6XF1, FHOD1-Nes2G complex and 6XF2, FHOD1-Nes1G complex.

EXPERIMENTAL MODEL AND SUBJECT DETAILS

Bacterial culture.—The bacterial strains used in generating proteins and the source of genetic materials used to produce protein of interest for this study are listed in Key Resource Tables. The details of bacterial growth and induction condition are described in Method Details section.

Cell culture.—Male NIH3T3 fibroblasts were maintained in Dulbecco's Modified Eagle Medium (DMEM) containing 10 mM HEPES pH 7.4 and 10% (v/v) bovine calf serum. 293T cells were maintained in DMEM containing 10 mM HEPES pH 7.4 and 5% (v/v) bovine calf serum and 5% (v/v) fetal bovine serum.

METHOD DETAILS

Plasmids—All constructs were confirmed by DNA sequencing. For all protein expressions in bacteria, except for human Rac1, pETDuet1 vector (Novagen) derivatives were used with either a human rhinovirus 3C (3C)-cleavable His-tag or MBP tag. Human Rac1 in pGEX-2T was purchased from Addgene (Catalog No. 12200) and modified by replacing the existing thrombin cleavage site with a 3C cleavage site. A G12V (GGA to GTA) mutation was introduced to produce constitutively active Rac1. For *in vivo* experiments, several plasmids were generated. pSUPER-hygro was derived from the pSUPER-puro (Oligoengine) by replacing a puromycin resistance gene sequence with a hygromycin resistance gene sequence from pMSCV-hygro vector (Clontech), and it was used for expressing shRNA in NIH3T3 fibroblasts by retroviral infection. pMSCV-puro EGFP-C4 vector (Antoku et al., 2019) was used to express EGFP tagged FHOD1 in NIH3T3 by retrovial infection. pLV-EF1a EGFP-C4 vector (Antoku et al., 2019) was used to express EGFP tagged Nes2G fragment in NIH3T3 by lentiviral infection. pMYC-C4 vector (Antoku et al., 2019) was used to express myc-tagged FHOD1 by microinjection. Human FHOD1 wild-type, I705A and human FHOD1 1–339 (wtFHOD1-N) sequences were previously described (Kutscheidt et al., 2014). The coding sequence for human Nes2G SR11–12 (residue 1425–1649) was generated by PCR from HEK293T cell cDNA while the coding sequences for human FHOD1 DAD (1052–1164), human Nes1G SR17–18 (residues 1976–2200), and human Nes1G SR18 (residues 2076–2200) were synthesized (Genewiz).

Human FHOD1 1–339 C31S C71S, mtFHOD1-N (TGT/TGT to AGT/AGT), FHOD1 R136A R137A (CGCCGC to GCCGCC), FHOD1 E36A P37G R38A (GAGCCGCGC to GCAGGGGCA), Nes1G SR17–18 D2176A D2180 (GAC/GAT to GCC/GCT), and Nes2G SR11–12 D1625A D1629A (GAT/GAT to GCT/GCT) mutants were made by introducing point mutations. For biotinylation, Nes1G and Nes2G were N-terminally tagged with the AVI sequence (GLNDIFEAQKIEWHE). The FHOD1 coding DNA was inserted into pETDuet1-His, pETDuet1-MBP, pMSCV-puro EGFP-C4, or pMYC vector. The Nes1G and Nes2G constructs were inserted into pETDuet1 or pEGFP-C4 vector (Antoku et al., 2019).The shRNA sequence for NC and FHOD1 is 5'-caacaagatgaagagcaccaa-3' and 5'-gaacctctttcctaccatttc-3', respectively.

Protein expression and purification—LOBSTR(DE3)-RIL *E. coli* cells (Kerafast) were transformed with the Nes2G SR11–12 expression vector and grown at 37 °C in LB medium with 0.4% (w/v) glucose and in the presence of antibiotics to maintain the plasmids. Protein expression was induced with 0.2 mM isopropyl β D-1-thiogalactopyranoside (IPTG) at OD600 = 0.7, at which point the culture was shifted to 18 °C. Cells were grown for another 12–16 h. The cells were then harvested by centrifugation at 6000 g for 6 mins and resuspend in 50 mM potassium phosphate pH 8.0, 400 mM NaCl, 40 mM imidazole and 5 mM β-mercaptoethanol. Cells were lysed by mechanical disruption with a LM-20 Microfluidizer (Microfluidics) at 18,000 psi then spun at 9500 g for 25 mins. The clear supernatant was incubated with Ni-Sepharose 6 Fast Flow (GE Healthcare) to capture the His-tagged protein. After batch washing in lysis buffer, the Ni-resin was poured into a disposable column, drained, and the bound protein was eluted with elution buffer (10 mM Tris/HCl pH 7.5, 150 mM NaCl, 250 mM imidazole, 5 mM β-mercaptoethanol). The eluate was cleaved with 3C protease overnight and Nes2G SR11–12 was further purified by cation exchange chromatography on a HiTrap SP-FF column (GE Healthcare).

FHOD1-N expression and purification were carried out as for Nes2G SR11–12 described above. To form complexes, purified Nes2G SR11–12 and wt FHOD1-N or mt FHOD1-N were mixed in a 1 to 1 ratio followed by size exclusion chromatography. The protein complex eluted as a monodisperse peak from a Superdex 200 gel filtration column (GE Healthcare) in 20 mM HEPES/NaOH pH 8.0, 100 mM KCl, 0.2 mM EDTA, 1 mM DTT. All remaining Nes2G SR11–12 mutants (L1628R, L1628A E1632A, D1625A D1629A) and FHOD1-N mutants (R136A R137A, E36A P37A R38A) were expressed and purified with the same protocol.

FHOD1 DAD domain (residue 1052–1164) preceded by maltose binding protein (MBP) and a 3C-cleavage site was expressed the same way. The sample in lysis buffer 10 mM HEPES/NaOH pH 8.0, 200 mM KCl, 5 mM β-mercaptoethanol was purified by affinity chromatography over amylose resin. The target protein was eluted with 10 mM maltose and further purified via gel filtration on a Superdex S75 (GE Healthcare) column.

For affinity measurements by bio-layer interferometry, AVI tagged Nes1G and Nes2G were biotinylated in the *E. coli* expression host grown in media supplemented with 1 mM biotin.

The GST-tagged Rac1 G12V was expressed in the same way as FHOD1-N and Nesprin SRs. The cells were lysed in GST Lysis buffer: 50 mM Tris pH 7.5, 300 mM NaCl, 0.1 mM EDTA, 5 mM β-mercaptoethanol. The clarified lysate was injected into a 5 mL GST-HiTrap FF (GE Healthcare) column and the protein of interest was eluted with 10 mM reduced Glutathione. Then, the protein was dialyzed overnight back into GST Lysis buffer in the presence of 3C protease at 4°C. Finally, Rac1 G12V was separated from its cleaved GST tag by a 5 mL GST-HiTrap FF.

Purified Rac1 G12V was incubated with 10-fold excess of GMP-PNP (Sigma Aldrich) in molar ratio, 4 U calf intestinal phosphatase per mg of Rac1 and 200 mM final concentration of ammonium sulfate overnight at 4°C. Finally, the mixture of Rac1 G12V, GMP-PNP, CIP and ammonium sulfate were loaded on Sephadex 75 10/300 gel filtration column in 20 mM Tris pH 7.5, 100 mM NaCl, 5 mM $MgCl_2$, 1 mM DTT. Construct of Rac1 G12V with C-terminus AVI-tagged is expressed, purified and prepared with GMP-PNP in the same manner as described above.

Crystallization—Purified complexes of Nes2G SR11–12 with wtFHOD1-N or mutant FHOD1-N were concentrated to 7 mg/ml for sparse matrix crystallization screen. Both complexes initially crystallized in 0.1 M Tris/HCl pH 8.5, 0.2 M potassium sodium tartrate, 21% PEG 3350 at 18 °C using the hanging-drop vapor diffusion method with a 1 μL well-solution to 1 μL protein setup. Large, rectangular-rod crystals formed within 5 days and were supplemented with 15% glycerol as cryo-protectant prior to freezing. Crystals of Nes1G SR17–18 and FHOD1-N were grown in 0.1 M HEPES/NaOH pH 7.0, 0.2 M sodium thiocyanate, 40% 5/4 pentaerythritol propoxylate at 18 °C using the sitting drop method.

Data collection and processing—Diffraction data were collected at the NE-CAT beamline 24-ID-C in Argonne National Laboratory and processed with HKL-2000 (Otwinowski and Minor, 1997). The structures were all solved by molecular replacement using Phaser from within the PHENIX package (Liebschner et al., 2019). The initial search model was FHOD1-N (PDB Code 3DAD) (Schulte et al., 2008). Additional helical density for the spectrin repeats was readily visible in the initial map. The model was built and refined iteratively using COOT(Emsley et al., 2010) in combination with phenix.refine. The structure of Nes1G SR17–18 in complex with wtFHOD1-N were phased with molecular replacement of the Nes2G SR11–12 FHOD1-N complex structure. Table 1 lists the final statistics for two complexes, Nes2G SR11–12 - FHOD1-N and Nes1G SR17–18 - FHOD-N respectively.

Complex analysis by size exclusion chromatography—Purified proteins were mixed in a 2 to 1 molar ratio, with Nes1G or Nes2G in excess, and incubated on ice for 1hr. Then, 1 mL of sample mixture was loaded onto a Superdex S200 10/300 GL gel filtration column for size analysis. The running buffer for all analytical studies was 20 mM HEPES/NaOH pH 8.0, 100 mM KCl, 0.2 mM EDTA, 1 mM DTT. The chromatography experiment was run at 0.5 ml/min flow rate and 500 μL sample fractions were collected for SDS-PAGE analysis.

Bio-layer interferometry—Interaction of Nes1G or Nes2G spectrin repeats with FHOD1 was measured by Bio-layer interferometry on an 8-channel Octet RED96e system (Forté Bio). First, streptavidin biosensor tips were pre-incubated with an assay buffer (20 mM HEPES/NaOH pH 8.0, 100 mM KCl, 0.2 mM EDTA, 1 mM DTT, 0.2% bovine serum albumin (BSA) and 0.01% Tween-20) for 10 min at 30 °C. Then, the tips were incubated with N-terminally biotinylated Nes1G and Nes2G constructs in assay buffer to yield a loading thickness of 0.3–0.4 nm. After washing the tips with assay buffer binding to wtFHOD1-N was measured in real time by recording the increase in optical thickness of the tips during an association phase. Finally, the tips were transfer back into assay buffer to measure the dissociation rate. The concentration of FHOD1 was fixed at 0.4 μM for qualitative experiment to validate the effect of mutant versus wild-type Nes1G and Nes2G binding. A two-fold dilution series of FHOD1-N concentration ranging from 0.01 to 0.4 μM was used for measuring the binding affinity of FHOD1 and Nesprins.

Meanwhile the binding of C-terminally biotinylated Rac1 G12V (GMP-PNP) was tested with 2.5 μM, 5 μM and 10 μM of FHOD1-N respectively in the assay buffer supplemented with 2 mM GMP-PNP. To complement our findings, the interaction of biotinylated Nes2G SR11–12 or Nes1G SR17–18 with FHOD1-N (0.4 μM) was observed in the presence of 10-fold molar excess of Rac1 G12V (GMP-PNP) (4 μM). We used Octet Data Analysis software for data analysis and transferred the processed output into GraphPad Prism 7 for curve-fitting by using association-dissociation non-linear regression model.

DAD helix binding with Nes2G and FHOD1-N—Purified MBP-DAD was mixed with either wtFHOD1-N only or Nes2G SR11–12-FHOD1-N complex in a 1 to 1 molar ratio and incubated overnight in the presence of 3C protease. The samples were analyzed by gel filtration over Superdex S75 10/300 in running buffer 20 mM HEPES/NaOH pH 8.0, 100 mM KCl, 0.2 mM EDTA and 1 mM DTT. Relevant elution fractions were analyzed by SDS PAGE.

Analytical ultracentrifugation—FHOD1-N (2 mg/mL) was dialyzed into 20 mM HEPES/NaOH pH 8.0, 100 mM KCl, 0.2 mM EDTA with and without 0.5 mM Tris (2-carboxyethyl) phosphine hydrochloride (TCEP-HCl) for two days in 4 °C. Samples were then prepared in 450 μL with final concentrations of 0.3 mg/mL, 0.6 mg/mL and 0.8 mg/mL for sedimentation velocity (SV) experiment. The experiment was performed in an Optimal XL1 (Beckman Coulter) ultracentrifuge using the An50 Ti rotor at 20 °C with a rotation speed of 45,000 rpm. A total of 500 absorbance scans at 280 nm were acquired with 1-minute intervals. Scans 1 to 50 were used for analysis in SEDFIT (Brown and Schuck, 2006) with the continuous distribution c(S) model. SEDNTERP were used to calculate the density and viscosity of the buffer at 20 °C.

Virus production, infection, and drug selection—293T cells were transfected with retroviral vectors and pantropic packaging plasmids. Medium containing the produced virus was harvested 24 hours after transfection, added to the NIH3T3 fibroblasts in the presence of 2 μg/ml polybrene and incubated for one day. The infected cells were selected with 300 μg/ml hygromycin B and 1.5 μg/ml puromycin for one week. The cells were recovered from drug treatment for one additional week before used for the experiments.

Microinjection—For microinjection, each plasmid was suspended in 150 mM KCl and 10 mM HEPES pH 7.4 at 50 ng/μl and the plasmid injected in the nucleus of the cells. After 1.5 hours, cells were either stimulated and fixed or fixed for analysis.

Immunofluorescence microscopy—For indirect immunofluorescence microscopy, cells were fixed with 4% paraformaldehyde in phosphate-buffered saline (PBS) for 20 min, and permeabilized and blocked with PBS containing 0.1% Triton-X and 1% BSA for 30 min. The cells were labeled first with primary antibodies. These primary antibodies are mouse anti-myc (0.1 μg/ml), chicken anti-GFP (5 μg/ml), mouse anti-beta-catenin (1.25 μg/ml), mouse anti-pericentrin (2.5 μg/ml), and rat anti-tyrosinated-alpha-tubulin (1:40). After primary antibodies incubation, secondary antibodies (7.5 μg/ml) and DAPI (4 μg/ml) with or without Alexa-Fluor 647 conjugated phalloidin (66 nM) were applied. Lumencor light engine (Lumencor) and pE-300^{white} (CoolLED) light sources were used to excite fluorophore. TIRF 405/488/461/630 nm quad band set emission/excitation filter (Chroma Technology Corporation) was used to collect the light from DAPI, Alexa-Fluor 568, and Alexa-Fluor 647. GFP ET emission/excitation filter (Nikon) was used to collect the light from Alexa-Fluor 488. Images were acquired with a 40× PlanApo objective, NA 1.0 (Nikon) or 60× PlanApo TIRF objective, NA 1.49 (Nikon) and DS-Qi2 (Nikon) on a Nikon Eclipse Ti microscope (Nikon) controlled by Nikon's NIS-Elements software.

Western blotting—For western blotting, proteins suspended in SDS sample buffer were separated by SDS-PAGE. The proteins were transferred to nitrocellulose blots, probed with primary antibodies. These primary antibodies are rabbit anti-FHOD1 (0.2 μg/ml), mouse anti-GFP (0.2 μg/ml), and rat anti-tyrosinated-alpha-tubulin (1:2000) antibodies. These primary antibodies were detected either by chemiluminescence from HRP-conjugated secondary antibody (0.08 μg/ml) with Odyssy Fc (LI-COR Inc.) or infrared fluorescence from IRDye 680 or 800 conjugated secondary antibody (0.2 μg/ml) with Odyssy CLx (LI-COR Inc.).

LPA stimulation—A day before serum-starvation, NIH3T3 fibroblasts were plated on acid-washed coverslips. The next day, cells at about 40% confluency on coverslips were washed three times with DMEM and then DMEM containing 10 mM HEPES pH 7.4 and 0.1% (v/v) fatty acid free bovine serum albumin (Sigma-Aldrich, A7906) was added. After two days serum-starvation, the cells were stimulated with 10 μM LPA (Avanti Polar Lipids, 857130P) and fixed after 2 hours.

Quantification and Statistical Analysis: The position of centrosome relative to the axis between the nuclei and the leading edge was analyzed from images of DAPI, tubulin and β-catenin/pericentrin antibody-labeled cells as previously described (Gomes et al., 2005; Palazzo et al., 2001). Nuclear and centrosomal positions of NIH3T3 fibroblasts were determined from images using Cell Plot software (Chang et al., 2016).

Statistical analysis of data on centrosome reorientation was assessed by Chi-square test using GraphPad Software. Statistical evaluation of the position of the nucleus and centrosome in NIH3T3 fibroblasts was by one-way ANOVA followed by Tukey's multiple

comparison test using SAS University Edition. All evaluated data were from at least N=3 experiments.

Supplementary Material

Refer to Web version on PubMed Central for supplementary material.

ACKNOWLEDGEMENTS

Research was supported by the US National Institutes of Health (NIH) under grant number R01-AR065484 (T.U.S.), T32GM007287 (V.E.C.) and R35-GM136403 (G.G.G). The X-ray crystallography work was conducted at the Northeastern Collaborative Access Team beamlines, which are funded by the National Institute of General Medical Sciences from the NIH (P30 GM124165). Use of the Advanced Photon Source is supported by the US Department of Energy, Office of Basic Energy Sciences, under contract no. DE-AC02-06CH11357.

REFERENCES

Antoku S, Zhu R, Kutscheidt S, Fackler OT, and Gundersen GG (2015). Reinforcing the LINC complex connection to actin filaments: the role of FHOD1 in TAN line formation and nuclear movement. Cell Cycle 14, 2200–2205. [PubMed: 26083340]

Antoku S, Wu W, Joseph LC, Morrow JP, Worman HJ, and Gundersen GG (2019). ERK1/2 Phosphorylation of FHOD Connects Signaling and Nuclear Positioning Alternations in Cardiac Laminopathy. Dev Cell 51, 602–616.e12. [PubMed: 31794718]

Aravind L, Anantharaman V, Balaji S, Babu MM, and Iyer LM (2005). The many faces of the helix-turn-helix domain: Transcription regulation and beyond. Fems Microbiol Rev 29, 231–262. [PubMed: 15808743]

Bargodia S, Taylor SJ, Creasy CL, Chernoff J, Cerione RA, (1995). Identification of a mouse p21Cdc42/Rac activated kinase. J Biol Chem 270 (39): 22731–7. [PubMed: 7559398]

Bechtold M, Schultz J, and Bogdan S (2014). FHOD proteins in actin dynamics--a formin' class of its own. Small GTPases 5, 11. [PubMed: 25483300]

Breitsprecher D, and Goode BL (2013). Formins at a glance. Journal of Cell Science 1–7. [PubMed: 23516326]

Brown PH, and Schuck P (2006). Macromolecular Size-and-Shape Distributions by Sedimentation Velocity Analytical Ultracentrifugation. Biophys J 90, 4651–4661. [PubMed: 16565040]

Calvi A, and Burke B (2015). LINC Complexes and Their Role in Human Disease. In eLS. John Wiley & Sons, Ltd.

Chang W, Antoku S, and Gundersen GG (2016). Wound-Healing Assays to Study Mechanisms of Nuclear Movement in Fibroblasts and Myoblasts. Methods Mol. Biol 255–267.

Crisp M, Liu Q, Roux K, Rattner JB, Shanahan C, Burke B, Stahl PD, and Hodzic D (2006). Coupling of the nucleus and cytoplasm: role of the LINC complex. The Journal of Cell Biology 172, 41–53. [PubMed: 16380439]

Duong NT, Morris GE, Lam LT, Zhang Q, Sewry CA, Shanahan CM, and Holt I (2014). Nesprins: tissue-specific expression of epsilon and other short isoforms. PLoS ONE 9, e94380. [PubMed: 24718612]

Emsley P, Lohkamp B, Scott WG, and Cowtan K (2010). Features and development of Coot. Acta Crystallographica. Section D, Biological Crystallography 66, 486–501. [PubMed: 20383002]

Gasteier JE, Madrid R, Krautkrämer E, Schröder S, Muranyi W, Benichou S, and Fackler OT (2003). Activation of the Rac-binding partner FHOD1 induces actin stress fibers via a ROCK-dependent mechanism. The Journal of Biological Chemistry 278, 38902–38912. [PubMed: 12857739]

Gomes ER, Jani S, and Gundersen GG (2005). Nuclear Movement Regulated by Cdc42, MRCK, Myosin, and Actin Flow Establishes MTOC Polarization in Migrating Cells. Cell 121, 451–463. [PubMed: 15882626]

Gundersen GG, and Worman HJ (2013). Nuclear Positioning. Cell 152, 1376–1389. [PubMed: 23498944]

Higgs HN (2005). Formin proteins: a domain-based approach. Trends Biochem Sci 30, 342–353. [PubMed: 15950879]

Higgs HN, and Peterson KJ (2004). Phylogenetic Analysis of the Formin Homology 2 Domain. MBoC 16, 1–13. [PubMed: 15509653]

Horn HF (2014). LINC complex proteins in development and disease. Curr Top Dev Biol 109, 287–321. [PubMed: 24947240]

Ipsaro JJ, and Mondragón A (2010). Structural basis for spectrin recognition by ankyrin. Blood 115, 4093–4101. [PubMed: 20101027]

Janin A, Bauer D, Ratti F, Millat G, and Méjat A (2017). Nuclear envelopathies: a complex LINC between nuclear envelope and pathology. Orphanet J Rare Dis 12, 147. [PubMed: 28854936]

Kühn S, Erdmann C, Kage F, Block J, Schwenkmezger L, Steffen A, Rottner K, and Geyer M (2015). The structure of FMNL2–Cdc42 yields insights into the mechanism of lamellipodia and filopodia formation. Nat Commun 6, 7088. [PubMed: 25963737]

Kutscheidt S, Zhu R, Antoku S, Luxton GWG, Stagljar I, Fackler OT, and Gundersen GG (2014). FHOD1 interaction with nesprin-2G mediates TAN line formation and nuclear movement. Nature Cell Biology 16, 708–715. [PubMed: 24880667]

Lammers M, Meyer S, Kühlmann D, and Wittinghofer A (2008). Specificity of Interactions between mDia Isoforms and Rho Proteins. J Biol Chem 283, 35236–35246. [PubMed: 18829452]

Li J, Chen K, Zhu R, and Zhang M (2020). Structural basis underlying strong interactions between ankyrins and spectrins. JMB 432, 3838–3850.

Liebschner D, Afonine PV, Baker ML, Bunkóczi G, Chen VB, Croll TI, Hintze B, Hung L-W, Jain S, McCoy AJ, et al. (2019). Macromolecular structure determination using X-rays, neutrons and electrons: recent developments in Phenix. Acta Crystallogr Sect D 75, 861–877.

Lindeman RE, and Pelegri F (2012). Localized Products of futile cycle/ lrmp Promote Centrosome-Nucleus Attachment in the Zebrafish Zygote. Curr Biol 22, 843–851. [PubMed: 22542100]

Luxton GWG, Gomes ER, Folker ES, Vintinner E, and Gundersen GG (2010). Linear Arrays of Nuclear Envelope Proteins Harness Retrograde Actin Flow for Nuclear Movement. Science 329, 956–959. [PubMed: 20724637]

Mellad JA, Warren DT, and Shanahan CM (2011). Nesprins LINC the nucleus and cytoskeleton. Current Opinion in Cell Biology 23, 47–54. [PubMed: 21177090]

Morimoto A, Shibuya H, Zhu X, Kim J, Ishiguro K, Han M, and Watanabe Y (2012). A conserved KASH domain protein associates with telomeres, SUN1, and dynactin during mammalian meiosis. J Cell Biology 198, 165–172.

Nezami AG, Poy F, and Eck MJ (2006). Structure of the Autoinhibitory Switch in Formin mDia1. Structure 14, 257–263. [PubMed: 16472745]

Noegel AA, and Neumann S (2011). The role of nesprins as multifunctional organizers in the nucleus and the cytoskeleton. Biochem Soc T 39, 1725–1728.

Otomo T, Tomchick DR, Otomo C, Machius M, and Rosen MK (2010). Crystal structure of the Formin mDia1 in autoinhibited conformation. PLoS ONE 5, e12896. [PubMed: 20927343]

Otwinowski Z, and Minor W (1997). Processing of X-Ray Diffraction Data Collected in Oscillation Mode. In Macromolecular Crystallography, Part A, pp. 307–326.

Palazzo AF, Cook TA, Alberts AS, and Gundersen GG (2001). mDia mediates Rho-regulated formation and orientation of stable microtubules. Nat Cell Biol 3, 723–729. [PubMed: 11483957]

Pruyne D (2017). Probing the origins of metazoan formin diversity: Evidence for evolutionary relationships between metazoan and non-metazoan formin subtypes. Plos One 12.

Rajgor D, and Shanahan CM (2013). Nesprins: from the nuclear envelope and beyond. Expert Rev Mol Med 15, e5. [PubMed: 23830188]

Rivero F, Muramoto T, Meyer A-K, Urushihara H, Uyeda TQ, and Kitayama C (2005). A comparative sequence analysis reveals a common GBD/FH3-FH1-FH2-DAD architecture in formins from Dictyostelium, fungi and metazoa. Bmc Genomics 6, 28. [PubMed: 15740615]

Romero S, Clainche CL, Didry D, Egile C, Pantaloni D, and Carlier M-F (2004). Formin Is a Processive Motor that Requires Profilin to Accelerate Actin Assembly and Associated ATP Hydrolysis. Cell 119, 419–429. [PubMed: 15507212]

Rothballer A, and Kutay U (2013). The diverse functional LINCs of the nuclear envelope to the cytoskeleton and chromatin. Chromosoma 122, 415–429. [PubMed: 23736899]

Schönichen A, Mannherz HG, Behrmann E, Mazur AJ, Kühn S, Silván U, Schoenenberger C-A, Fackler OT, Raunser S, Dehmelt L, et al. (2013). FHOD1 is a combined actin filament capping and bundling factor that selectively associates with actin arcs and stress fibers. J Cell Sci 126, 1891–1901. [PubMed: 23444374]

Schulte A, Stolp B, Schönichen A, Pylypenko O, Rak A, Fackler OT, and Geyer M (2008). The human formin FHOD1 contains a bipartite structure of FH3 and GTPase-binding domains required for activation. Structure 16, 1313–1323. [PubMed: 18786395]

Smith TF (2008). Diversity of WD-Repeat proteins. Subcell Biochem. 48, 20–30. [PubMed: 18925368]

Sosa BA, Rothballer A, Kutay U, and Schwartz TU (2012). LINC Complexes Form by Binding of Three KASH Peptides to Domain Interfaces of Trimeric SUN Proteins. Cell 149, 1035–1047. [PubMed: 22632968]

Starr DA, and Fridolfsson HN (2010). Interactions between nuclei and the cytoskeleton are mediated by SUN-KASH nuclear-envelope bridges. Annual Review of Cell and Developmental Biology 26, 421–444.

Takeya R, and Sumimoto H (2003). Fhos, a mammalian formin, directly binds to F-actin via a region N-terminal to the FH1 domain and forms a homotypic complex via the FH2 domain to promote actin fiber formation. J Cell Sci 116, 4567–4575. [PubMed: 14576350]

Takeya R, Taniguchi K, Narumiya S, and Sumimoto H (2008). The mammalian formin FHOD1 is activated through phosphorylation by ROCK and mediates thrombin-induced stress fibre formation in endothelial cells. The EMBO Journal 27, 618–628. [PubMed: 18239683]

Zhang Q, Skepper JN, Yang F, Davies JD, Hegyi L, Roberts RG, Weissberg PL, Ellis JA, and Shanahan CM (2001). Nesprins: a novel family of spectrin-repeat-containing proteins that localize to the nuclear membrane in multiple tissues. Journal of Cell Science 114, 4485–4498. [PubMed: 11792814]

Highlights

- Nes2G SR11/12 FHOD1-N complex is structurally characterized at 2.8 Å resolution
- DxWLD[IVLA]xE motif in the spectrin repeat revealed as critical for FHOD1 interaction
- Disrupting Nes2G SR11/12 FHOD1-N interaction blocks nuclear migration
- FHOD1 N-terminal domain binds spectrin-repeats rather than GTPases

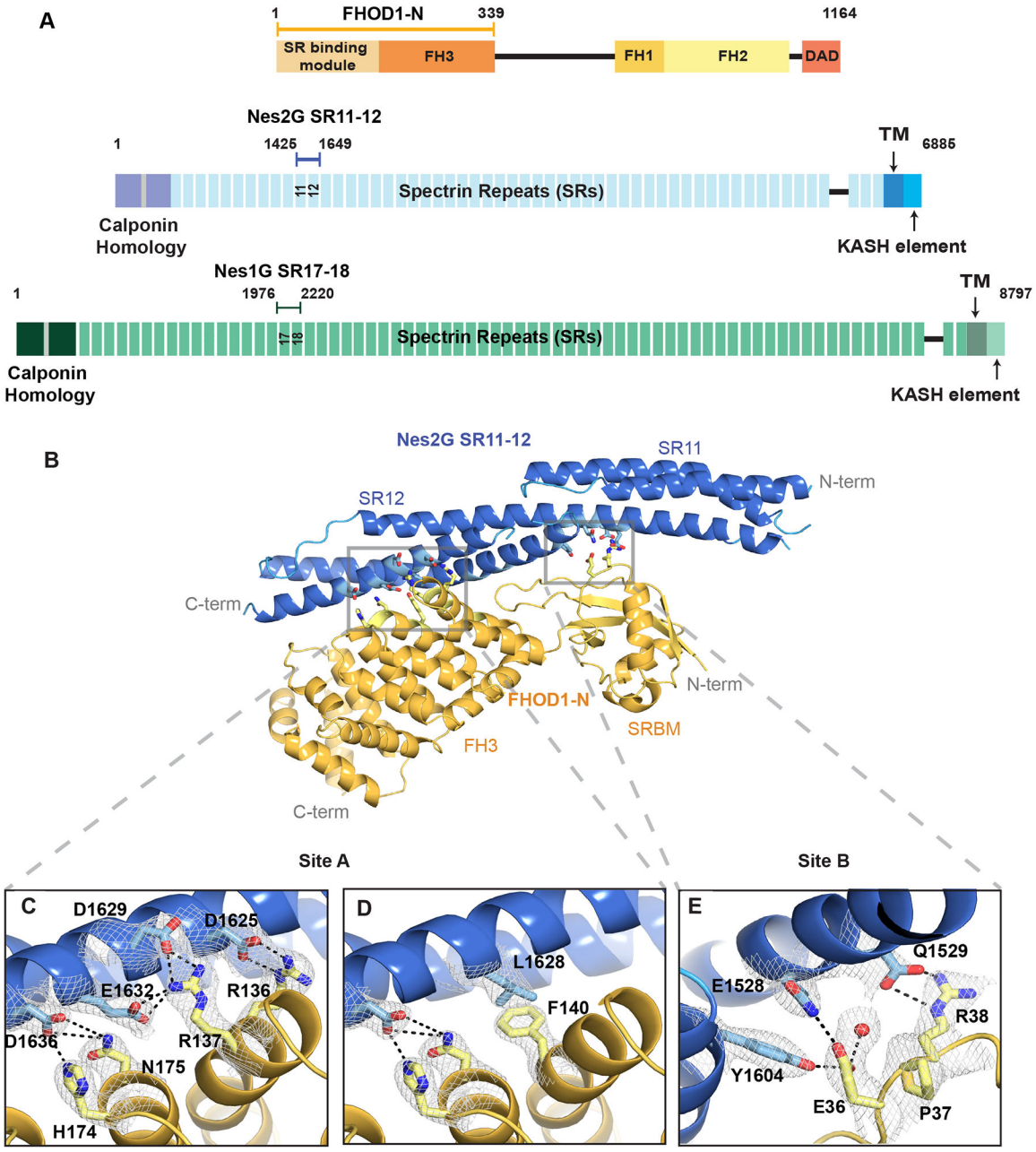

Figure 1.

Structure of the FHOD1-N and Nes2G SR11–12 complex

(A) Schematic diagram to show the boundaries of FHOD1-N, Nes2G SR11–12, and Nes1G SR17–18 fragments in the context of the full-length proteins. **(B)** Overall crystal structure of Nes2G SR11–12 bound to FHOD1-N with interface residues, as part of the main interaction sites A and B shown as sticks. Nes2G in blue, FHOD1 in orange. **(C, D)** Close-up views of key interaction sites within site A. Both show the same perspective, with different, otherwise overlapping residues, removed for clarity. H-bonds and charged interactions shown as black dashed lines. **(C)** emphasizes charged interactions, **(D)** shows a critical hydrophobic

interaction. **(E)** Close-up view of site B dominated by the $EPR_{36–38}$ element of the SRBM of FHOD1. A water molecule in red.

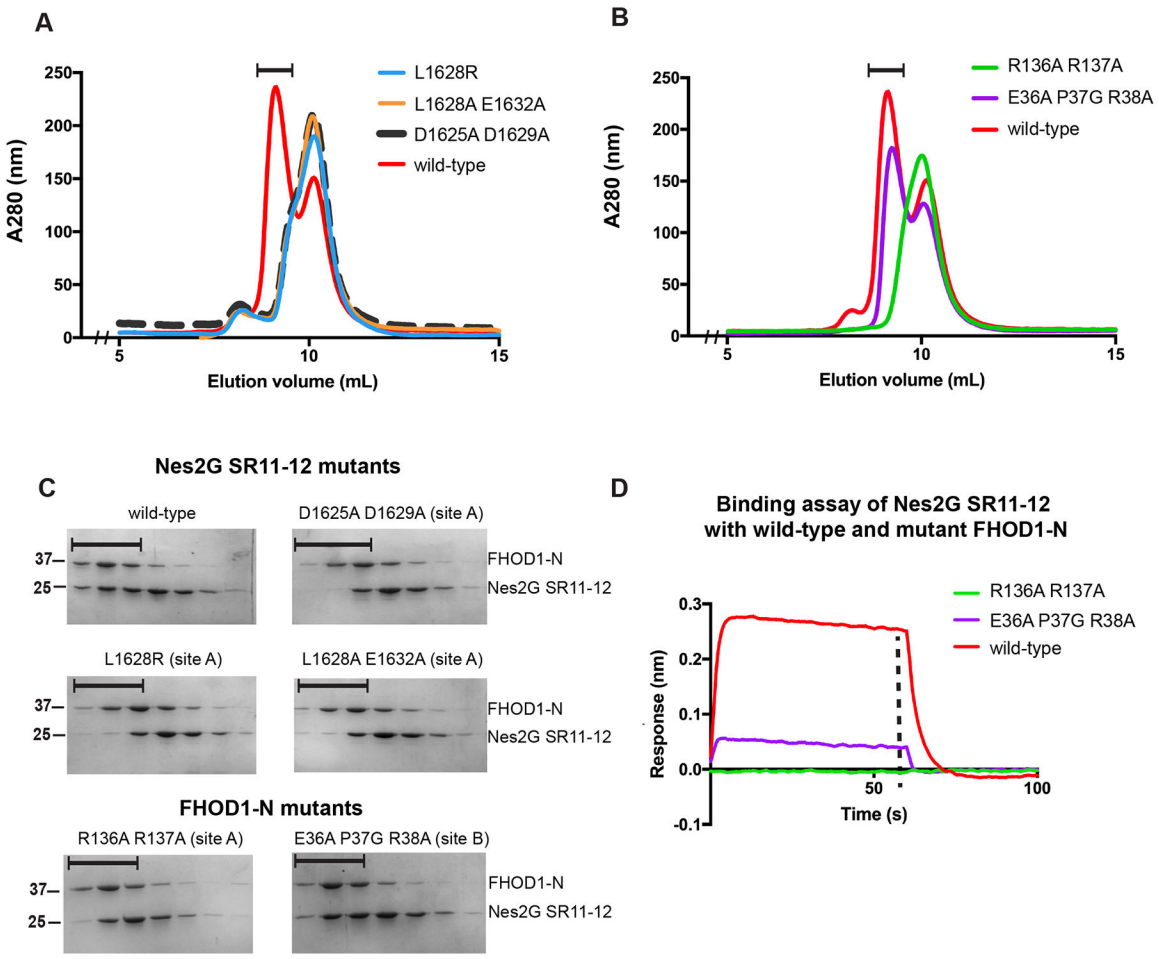

Figure 2:

Analysis of residues involved in FHOD1-N-Nes2G SR11–12 complex formation. **(A)** Size exclusion chromatography (SEC) profile of purified FHOD1-N incubated with wild-type Nes2G SR11–12, or mutant variants. Only the wild-type stably binds. **(B)** Complementary experiment with Nes2G SR11–12, and wild-type or mutant FHOD1-N fragments. Both experiments were carried out on a Superdex S75 10/300 column. **(C)** SDS-PAGE analysis of the SEC elution fractions (black bars) in A and B. **(D)** Binding activity of the two proteins with Biolayer interferometry (BLI) where Nes2G SR11–12 is immobilized as ligand, and tested against the indicated analytes. The dashed vertical line indicates the beginning of the dissociation phase.

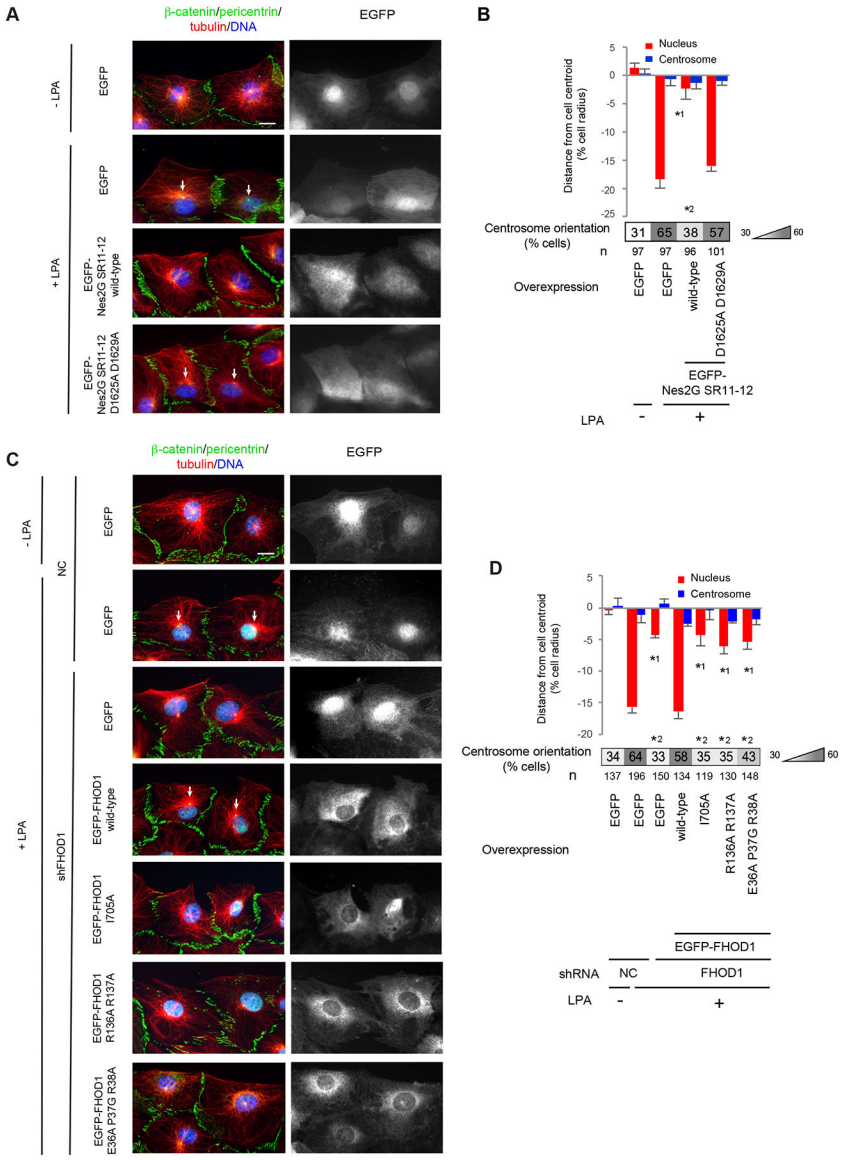

Figure 3:

Effects of FHOD1-Nes2G interaction site mutants on nuclear movement and centrosome orientation. **(A)** Images of LPA-stimulated wounded edge NIH3T3 fibroblasts expressing either EGFP or EGFP-tagged Nes2G SR11–12s and immunostained for the indicated proteins and nuclei (DAPI). White arrows, oriented centrosomes. **(B)** Quantification of nuclear and centrosome position relative to the cell centroid for cells treated as in A. Centrosome orientation is shown in the heat map below the histogram. **(C)** Images of LPA-stimulated wounded edge NIH3T3 fibroblasts depleted of FHOD1 with shRNA (shFHOD1) and re-expressing either EGFP or EGFP-tagged FHOD1 proteins. Cells were immunostained for the indicated proteins and nuclei (DAPI). White arrows, oriented centrosomes. **(D)** Quantification of nuclear and centrosome position relative to the cell centroid for cells treated as in C. Centrosome orientation is shown in the heat map below the histogram. Values are means ± SEM; n, cells examined. Centrosome orientation (mean % of cells), is

shown in the heat map below the histograms. $*^1$ and $*^2$ indicate $p < 0.01$ compared to the LPA-stimulated control to the rest of the samples for each category.

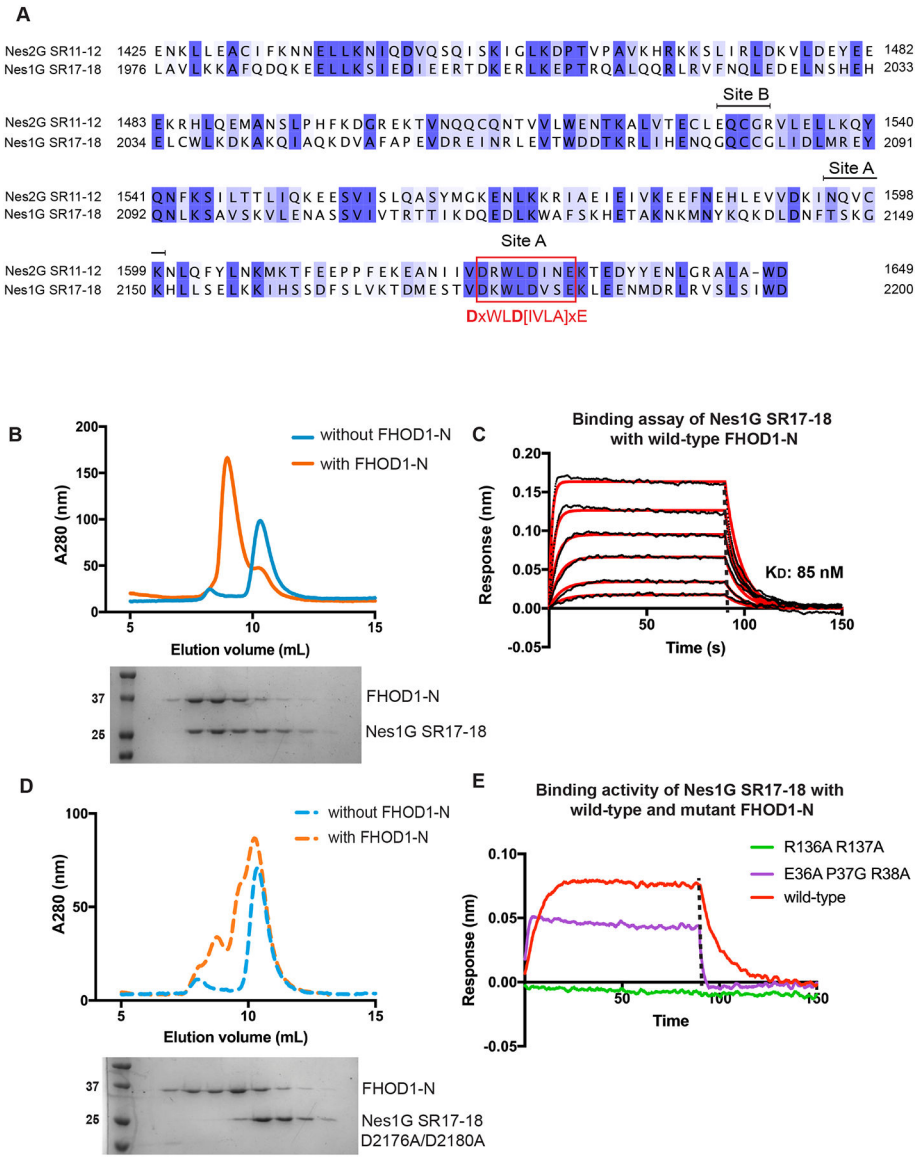

Figure 4:

Nes1G SR17–18 is another FHOD1-binding spectrin repeat.

(A) Sequence alignment of the two tandem SRs that have a matching sequence pattern indicative of FHOD1 binding. The search sequence is shown below the alignment. Interface residues involved in site A and site B are labelled and the critical motif is boxed in red. **(B)** SEC profile of Nes1G SR17–18 incubated with or without FHOD1-N, with SDS PAGE analysis of the eluted fractions. **(C)** BLI binding assay of Nes1G SR17–18 and FHOD1-N. Individual curves represent a 2-fold dilution series from a maximal concentration of 400 nM **(D)** Setup as in **(B)** but using mutant Nes1G SR17–18 D2176A D2180A instead of wild-type. Both SEC experiments were performed on a Superdex S75 10/300 column. **(E)** Binding assay of wild-type and mutant FHOD1-N with Nes1G SR17–18 measured by BLI.

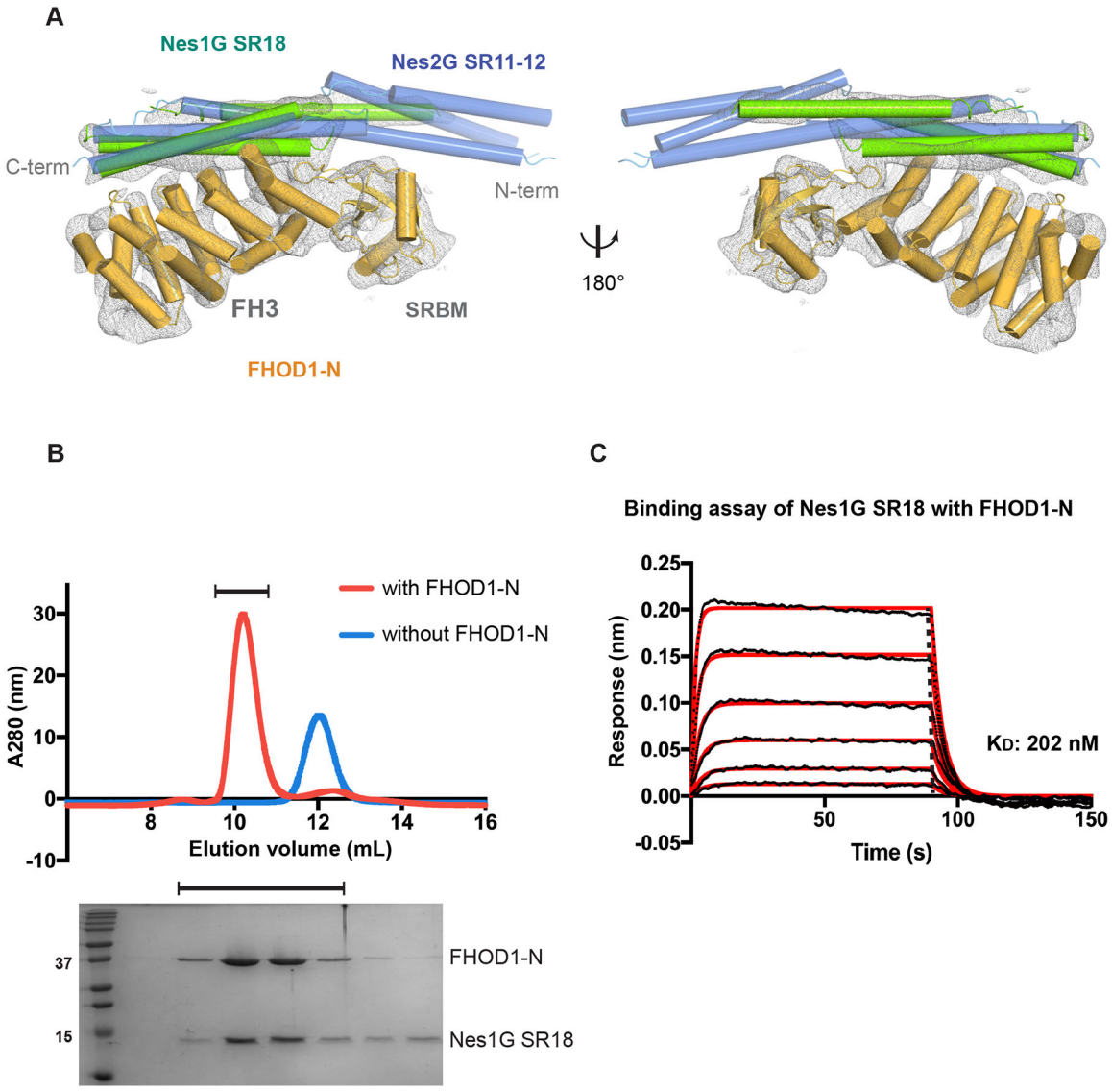

Figure 5:

SR18 of Nes1G is sufficient to bind FHOD1-N.

(A) Crystal structure of FHOD1-N bound with Nes1G SR17–18 at 7.0 Å resolution with 2Fo-Fc map contoured at 1.2 sigma. SR17 was not modeled because of insufficient electron density. Nes2G SR11–12 (blue) overlaid for comparison. **(B)** SEC experiment of Nes1G SR18 with or without FHOD1-N, accompanied by SDS-PAGE analysis of the eluted fractions. **(C)** Binding of Nes1G SR18 with FHOD1-N measured by BLI.

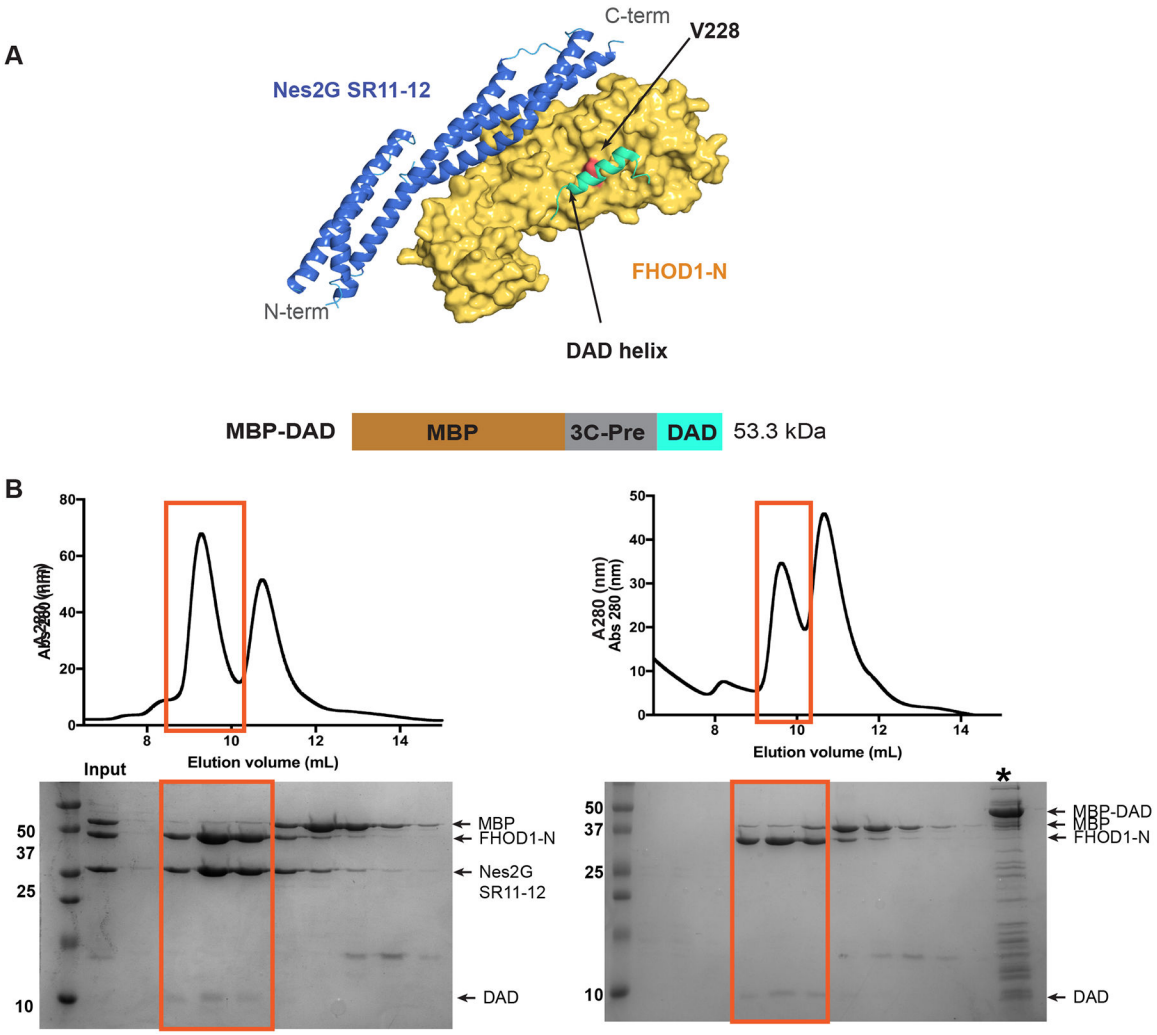

Figure 6:

SR binding to FHOD1 does not sterically compete with DAD autoregulatory binding. **(A)** The Nes2G SR11–12-FHOD1-N complex overlaid with the DAD helix (cyan). The DAD helix was positioned based on an alignment with the mDia-FH3 domain bound to its DAD helix (PDB code 2F31). FHOD1-V228, critical for DAD-binding in deep-orange. **(B)** Analytical SEC of MBP-DAD with Nes2G SR11–12 and FHOD1-N complex (left panel) or FHOD1-N alone (right panel) in the presence of 3C protease. A Superdex S75 10/300 GL column was used in all the SEC experiments. Uncleaved MBP-DAD (*) was run as a control.

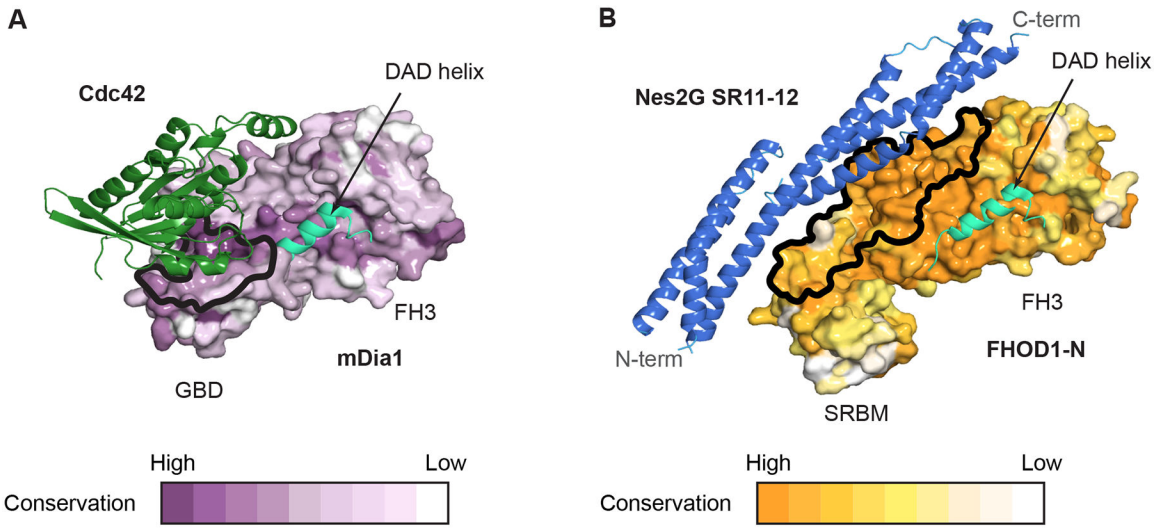

Figure 7:

Modulation of the FH3 binding activity by its N-terminally paired domain

(A) Comparison between GBD-FH3 of mDia1 bound to the small GTPase Cdc42 and **(B)** SRBM-FH3 of FHOD1 bound to Nes2G SR11–12. Structures are aligned using the FH3 domain. Binding surfaces outlined. Paired SRBM- or GBD-FH3 domains shown as surfaces, gradient-colored according to conservation as indicated. DAD helix position modeled (cyan). SR and small GTPase bind in mutually exclusive positions. Surfaces are specifically conserved to recognize either SR or small GTPases, defining a difference between the two classes of formins.

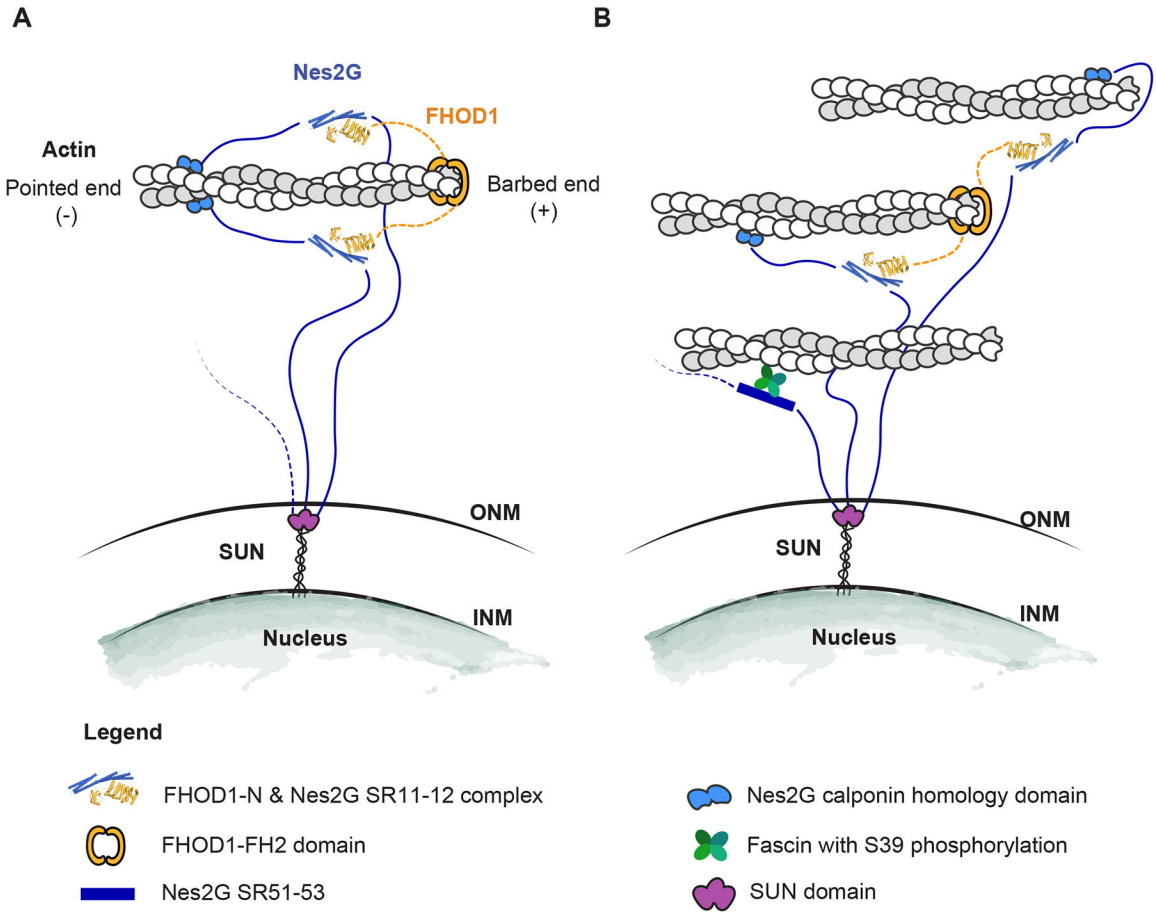

Figure 8:

Model of LINC connection with cytoplasmic actin bundles.

A cartoon depiction of the SUN-Nes2G FHOD1-actin model. FHOD1 binds to the barbed end of long actin polymer where its association with Nes2G can either **(A)** enforce binding of LINC to a single actin filament or **(B)** play a part in the bundling of actin cables.

Table 1.

Data collection and refinement statistics (molecular replacement)

	Human Nes2G SR11–12$_{1425–1649}$ FHOD1$_{1–339}$ 6XF1	Human Nes1G SR18$_{1976–2200}$ FHOD1$_{1–339}$ 6XF2
Data collection		
Space group	C 2	C 2
Cell dimensions		
a, *b*, *c* (Å)	237.8, 52.4, 117.5	209.4, 142.1, 58.1
α, β, γ (°)	90.0, 123.3, 90.0	90.0, 106.3, 90.0
Resolution (Å)	67.3 – 2.8 (2.9 – 2.8)	60.6 – 7.1 (7.3 – 7.1)
R_{pim}	0.07 (1.3)	0.06 (0.52)
I / σ(I)	21.6 (1.9)	15.7 (1.1)
$CC_{1/2}$	0.54	0.98
Completeness (%)	98.9 (97.9)	97.7 (94.5)
Total reflections	50981	2388
Unique reflections	8641	398
Redundancy	5.9	6.0
Refinement		
Resolution (Å)	67.3 – 2.8	60.6 – 7.1
No. reflections	45286	2378
R_{work} / R_{free}	0.22 / 0.26	0.33 / 0.39
No. atoms	8580	6075
Protein	8556	6075
Ligand/ion		
Water	24	
***B*-factors (Å^2)**		
Protein	78	464
Ligands/ion		
Water	69	
r.m.s. deviations		
Bond lengths (Å)	0.01	0.01
Bond angles (°)	1.9	1.7
Ramachandran analysis		
Favored (%)	96.5	96.7
Allowed (%)	2.4	3.1
Outliers (%)	1.1	0.2

*Values in parentheses are for highest-resolution shell.

KEY RESOURCES TABLE

REAGENT or RESOURCE	SOURCE	IDENTIFIER
Antibodies		
Mouse monoclonal GFP antibody	Santa Cruz Biotech	Cat# sc-9996, RRID: AB_627695
Rabbit polyclonal FHOD1 antibody	Santa Cruz Biotech	Cat# sc-99209, RRID: AB_2104511
Rat polyclonal α-tubulin	European Collection of Authenticated Cell Cultures	Cat# 92092402
Chicken polyclonal GFP antibody	EMD Millipore	Cat# AB16901, RRID: AB_90890
Mouse monoclonal β-catenin	Thermo Fisher Scientific	Cat# 13-8400, RRID: AB_2533039
Mouse monoclonal pericentrin	BD Biosciences	Cat# 611814, RRID: AB_399294
Mouse monoclonal myc	Sigma Aldrich	Cat# 11667149001, RRID: AB_390912
Rat polyclonal myc	Santa Cruz Biotech	Cat# sc-789; RRID: AB_631274
Alexa Fluor 488 conjugated donkey anti-chicken IgY	Jackson Immuno Research Laboratories	Cat# 703-546-155, RRID: AB_2340376
Alexa Fluor 488 conjugated donkey anti-mouse IgG	Jackson Immuno Research Laboratories	Cat# 715-545-150, RRID: AB_2340846
Alexa Fluor 488 conjugated donkey anti-rabbit IgG	Jackson Immuno Research Laboratories	Cat# 711-545-152, RRID: AB_2313584
Alexa Fluor 647 conjugated donkey anti-rat IgG	Jackson Immuno Research Laboratories	Cat# 712-605-153, RRID: AB_2340694
Alexa Fluor 568 conjugated donkey anti-mouse IgG	Thermo Fisher Scientific	Cat# A10037, RRID: AB_2534013
HRP conjugated goat anti-rabbit IgG	Santa Cruz Biotech	Cat# sc-2005, RRID: AB_631736
IRDye 680 conjugated goat anti-mouse IgG	LI-COR Biosciences	Cat# 926-32220, RRID: AB_621840
IRDye 800CW conjugated goat anti-rat IgG	LI-COR Biosciences	Cat# 926-32219, RRID: AB_1850025
Bacterial and Virus Strains		
Escherichia coli, LOBSTR BL21(DE3) RIL	Kerafast	Cat# EC1002
Chemicals, Peptides, and Recombinant Proteins		
Alexa Fluor 647-phalloidin	Thermo Fisher Scientific	Cat# A22287
Lysophosphatidic acid (LPA)	Avanti Polar Lipids	Cat# 857130P
4′,6-diamidino-2-phenylindole (DAPI)	Thermo Fisher Scientific	Cat# D3571
Guanosine 5'-[β,γ - imido] triphosphate trisodiumsalt hydrate (GMP-PNP)	Sigma-Aldrich	Cat# G0635
Bovine serum albumin (BSA)	Sigma-Aldrich	Cat# A7906
Bovine calf serum	GE Health Life Science	Cat# SH30072.03
Fetal bovine serum	Gemini Bio-Products	Cat# 900-108
Calf Intestinal Phosphatase (CIP)	NEB	Cat# M0290
Polybrene	EMD Millipore	Cat# TR-1003
Hygromycin B	EMD Millipore	Cat# 400051
Puromycin	Sigma-Aldrich	Cat# P8833
Western Lightening Plus-ECL	PerkinElmer	Cat# NEL103001EA
32% Paraformaldehyde	Electron Microscopy Sciences	Cat# 15714
Dulbecco's Modified Eagle Medium (DMEM)	Corning Inc.	Cat# 10-017-CV

REAGENT or RESOURCE	SOURCE	IDENTIFIER
Human formin homology domain protein 1 (FHOD1)	This paper	UniprotKB: Q9Y613
Human Nesprin-2 (SYNE2)	This paper	UniprotKB: Q8WXH0
Human Nesprin-1 (SYNE1)	This paper	UniprotKB: Q8NF91
Deposited Data		
Human Nes2G-SR11-12$_{1425–1649}$ FHOD1$_{1–339}$	This paper	PDB: 6XF1
Human Nes2G-SR18$_{1976–2200}$ FHOD1$_{1–339}$	This paper	PDB: 6XF2
Human Formin Homology domain protein (1–339)	Schulte et al., 2008	PDB: 3DAD
Mouse mDia FH3-domain bound with DAD helix	Nezami et al., 2006	PDB: 2F31
Mouse mDia-TSH GBD-FH3 in complex with Cdc42-GMP PNP	Lammers et al, 2008	PDB: 3EG5
Human FMNL1 N-terminal domain bound to Cdc42	Kühn et al, 2015	PDB: 4YDH
Human erythroid β-spectrin bound to ankyrin	Ipsaro and Mondragón, 2010	PDB: 3KBT
Human brain alpha spectrin repeat 15 and 16	Vorobiev., SM et al 2008 (To be published)	PDB: 3FB2
AnkyrinB/β-spectrin complex	Li et al., 2020	PDB: 6M3Q
Experimental Models: Cell Lines		
NIH3T3	ATCC	Cat# CRL-1658, RRID: CVCL_0594
HEK293T	ATCC	Cat# CRL-3216, RRID: CVCL_0063
Oligonucleotides		
Primers used in this study, see Table S1	This paper	N/A
Recombinant DNA		
pETDUET-1-DNA	Novagen	Cat# 71146-3
pGEX-2T- human Rac1	Bargodia et al., 1995	Addgene Cat# 12200
pMSCV-puro EGFP-C4 vector	Antoku et al., 2019	N/A
pMSCV-puro EGFP-C4 human FHOD1 WT	Antoku et al., 2019	N/A
pMSCV-puro EGFP-C4 human FHOD1 I705A	This paper	N/A
pMSCV-puro EGFP-C4 human FHOD1 R136A R137A	This paper	N/A
pMSCV-puro-EGFP-C4 FHOD1 E36A P37G R38A	This paper	N/A
pMYC-C4 hFHOD1 1-1053	Antoku et al., 2019	N/A
pMYC-C4 hFHOD1 1-1053 R136A R137A	This paper	N/A
pMYC-C4 hFHOD1 1-1053 E36A P37G R38A	This paper	N/A
pLV EF1a EGFP-C4	Antoku et al., 2019	N/A
pLV EF1a EGFP-C4 Nes2G SR11-12	This paper	N/A
pLV EF1a EGFP-C4 Nes2G SR11-12 D1625A D1629A	This paper	N/A
pSUPER.retro.hygro shNC	Antoku et al., 2019	N/A
pSUPER.retro.hygro shFHOD1	Antoku et al., 2019	N/A

REAGENT or RESOURCE	SOURCE	IDENTIFIER
Software and Algorithms		
Cell Plot Software	Chang et al., 2016	https://changlab.fhs.um.edu.mo/software/cellplot/
SAS University edition	SAS	https://www.sas.com/en_us/software/university-edition.html
HKL2000 v720	Otwinowski and Minor., 1997	https://hkl-xray.com/
COOT- 0.9	Emsley et al., 2010	https://www2.mrc-lmb.cam.ac.uk/personal/pemsley/coot/
PHENIX - 1.18.2-3874	Liebschner et al., 2019	https://www.phenix-online.org/
Prism 7	GraphPad Software	https://www.graphpad.com/scientific-software/prism/
SEDFIT	Brown and Schuck., 2006	http://www.analyticalultracentrifugation.com/default.htm
OCTET Data Analysis Software	Forté Bio	https://www.fortebio.com/products/octet-systems-software